

Chapter 6

3D Nanometric Analyses via Electron Tomography: Application to Nanomaterials

Simona Moldovan, Raul Arenal, and Ovidiu Ersen

6.1 Introduction to 3D Imaging

In the last few years, the 3D exploration of the nanoworld has gained growing attention in the field of material science research, as a full knowledge of the morphology, structure and composition of nano-objects requires to be acquired in three dimensions. Numerous scientific and technological efforts have been devoted to the synthesis of nano-objects and/or nanostructured materials for conceiving new systems and components making use of nanomaterials with characteristics adapted for applications in various fields: electronics, catalysis, biotechnology, medicine, etc. In addition, more fundamental developments in material science research such as spintronics or plasmonics should be taken into account as major points for the development of complex nano-systems and/or nanocomposites. One of the main interests of developing nanomaterials originates in the necessity of synthesising materials with enhanced surface areas with respect to the bulk, as demanded for various applications. Ultimately, the close control of the structural, morphological and chemical characteristics of nanomaterials is imperative as they define and control the final system properties. The continuous requirement for qualitative and quantitative analysis of complex nanomaterials has made the material research community turn its attention towards techniques allowing the investigation of small volumes. Obviously to reach all these goals, synergy between synthesis, characterisation and final

S. Moldovan • O. Ersen (✉)

Institut de Physique et Chimie des Matériaux de Strasbourg (IPCMS),
UMR 7504 CNRS, 23 Rue du Loess, Strasbourg 67037, France
e-mail: ersen@ipcms.unistra.fr

R. Arenal

Advanced Microscopy Laboratory, Nanoscience Institute of Aragon,
University of Zaragoza, 50018 Zaragoza, Spain

ARAID Foundation, 50018 Zaragoza, Spain

properties should be reached. In this general context, there is a need for state-of-the-art techniques for assessing material characteristics at the nanoscale such as active specific areas or porosities and therefore qualifying structures and three-dimensional space relationship. We describe here the 3D characterisation methods based on electron tomography when developed in an electron transmission microscope, which allow the performance of qualitative and quantitative 3D analyses with a nanometric (even atomic) spatial resolution.

6.2 3D Characterisation Techniques: Electron Tomography, Atom Probe Tomography, FIB and Confocal Microscopy

Experimental techniques such as X-ray reflectivity, spectroscopic ellipsometry, small-angle X-ray scattering [SAXS or grazing incidence SAXS (GISAXS)] are widely employed to reveal the physical and chemical characteristics of materials in terms of structure, morphology and/or chemical composition. These techniques have the big disadvantage to furnish information only on the averaged volumes of the samples of interest and not on individual features. This drawback can be overcome by using near-field imaging techniques such as scanning tunnelling microscopy (STM), atomic force microscopy (AFM) or TEM, which are finely adapted for accessing information at the atomic level. The capabilities of probing very tiny surfaces with curvatures as small as possible situate the near-field and transmission electron microscopies on the other “extreme” of material characterisation. Another up-to-date technique for the 3D characterisation of materials is the atom probe tomography (APT). It allows for the achievement of the atomic resolution but can only explore very small volumes in a destructive manner and is not adapted for complex morphologies.

Before exploring deeper the electron tomography techniques, by highlighting their potentials, advantages and drawbacks, we will give a short overview of other methodologies currently available for the 3D analyses of materials, with resolutions ranging from micrometres down to nanometres. The X-rays attenuation when crossing a given material stands as the base principle of X-ray tomography. This attenuation strongly depends on the density of the material crossed by the incident ray and on the resolution attained of the order of micrometres or less when the experiments are carried out on synchrotrons. The confocal optical microscopy allows for the exploitation of volumes built up from slices acquired by optical microscopy with small depths of field. In the modern configurations, images are recorded by scanning the specimen using a laser beam and detecting the reflected or the fluorescence responses. After a scan, the next image is recorded deeper or higher from the specimen surface. This technique is well adapted for the 3D investigation of biological and/or soft materials, and it allows reaching a resolution down to 600 or even 200 nm. A more recent technique adapted for the study of hard materials is the APT. In principle, under the impact of a strong electric field, the atoms from the specimen surface evaporate one atomic layer after the other and their time of flight is measured. Finally, a mass-spectroscopy experiment is carried out allowing getting

a chemically selective 3D mapping at the atom scale. As compared with electron tomography, the main advantage of the atom probe technique is that APT close to the atomic resolution, even for amorphous materials, can be obtained. However, the main drawback remains its permanent damaging character. In addition, the specimen preparation is not straightforward, owing to the geometry restrictions imposed by the technique itself: the samples need to be shaped needlelike and the regions to be analysed have to be representative of the whole sample.

The electron tomography-based techniques imply the use of the two different modes: the transmission and the scanning electron microscopies (SEM). In the scanning mode, there are two ways for acquiring 3D images: the acquisition of a “tilted” series of projections under a SEM and the SEM-focused ion beam (FIB) tomography. The “tilted” mode under SEM implies the use of a specific specimen holder and the analysis of a relative thick specimen, and one reaches resolutions ranging from a micrometre to several tens of nanometre. The SEM-FIB implies the use of a dual-beam machine: a SEM equipped with an FIB. In principle, an ion beam is used to cut the object slice by slice, and the series of micrographs are successively acquired under SEM either by using the signal of the secondary/backscattered electrons or the X-ray photons.

In transmission electron microscopy (TEM), one might use as well two different methodologies for the 3D analysis of objects: the first mode, single particle analysis, relies on the object observation by acquiring one or several images at a given orientation, without tilting the specimen. The assumption is made that on one micrograph alone one captures all the possible orientations of the object. A condition that needs to be imperatively fulfilled is that all objects must be identical and belong to specific morphological and structural classes. This type of tomography is well adapted for biological samples, when several copies of a biochemically homogeneous specimen are available. It is thus frequently used for performing the reconstruction of specific molecules and viruses. Another possibility of 3D imaging by TEM tomography adaptable to all classes of nanomaterials and nano-objects implies acquiring a series of micrographs at different tilting angles, of a single specimen, and subsequent volume reconstruction and analysis.

In the present chapter, we will show that the electron tomography (or 3D-TEM) is an ideal tool that gives access to qualitative and quantitative information at the nanometre or even at the atomic level. When looking at a transparent and structured object, an observer does spontaneously rotate it in order to get a complete picture of the object. This idea stands as the principle of tomography: recording images at various given angles by employing the signal of some wave transmitted through the object of interest with a wavelength that limits the ultimate reachable resolution. Tomography generally uses light, sounds, neutrons, X-rays, etc. as probes as function of the size and the nature of the objects under investigation and information to inquest. In electron microscopy, the incident electrons with wavelengths in the picometre range are used as probe. They are therefore suitable for performing 3D imaging using the tomographic technique, with a nanometric resolution. When combined with chemical imaging (energy-filtered TEM), it gives access to the 3D chemical composition of nano-objects, which is a key issue for the subsequent analysis of the properties of interest.

6.3 Electron Tomography

Electron tomography is based on the recording of a series of projection images of an object rotated in the electron microscope for a well-defined number of incidence angles, in the range $\pm 80^\circ$ (or even 360° when a particular TEM holder is used). Each recorded image collects a projection in the observation plane of the quantity of interest: the mass or the chemical composition. In a second step, the Radon transformation [1] permits the construction of a 3D matrix, describing the sample in the real space. This is performed by the back-projection of the intensity of each corresponding pixel from the projections into a unique voxel of the matrix being constructed (Fig. 6.1).

Using the 3D voxel matrix constructed in this manner then allows to perform the quantitative or chemical analysis. A 3D imaging of the object of interest can be extracted from the matrix by recognising, through contrast measurements, the interface delimiting the vacuum and the matter in the case of shape-sensitive volumes. From this image, porosity, for example, can be quantitatively estimated with a nanometre-scale resolution as well as its distribution within the entire solid volume.

6.3.1 State of the Art

Electron tomography has been largely used in the second half of the last century as a powerful instrument for assessing the details of the morphology and the inner structures of living cells and molecular structures. The pioneering works of DeRosier and Klug [2] can be considered as the real starting points for the 3D imaging in electron microscopy. A brief history of the origin and the development of 3D

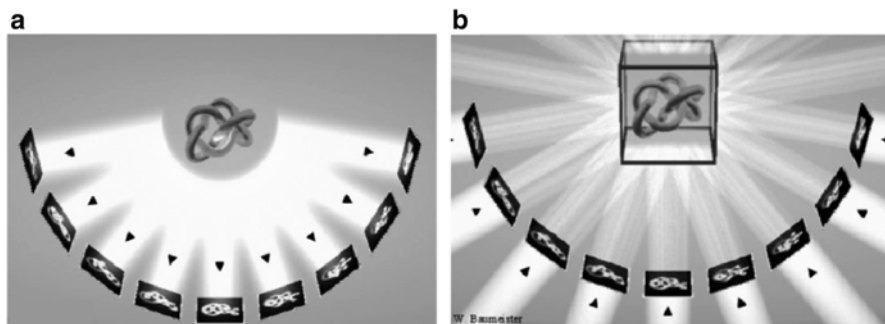


Fig. 6.1 Principle of electron tomography. (a) The projection: a set of projections recorded for a wide range of angles of rotation. (b) The back-projection: the intensity of each pixel from the projections is distributed along segments orthogonal to the recording plane. The summed intensity at the crossing point defines the intensity of one voxel within the reconstructed 3D object. Reprinted from Medalia et al. [4]

reconstruction methods is given in the Nobel Lecture of Klug in 1983 [3]. The work published by Medalia et al. [4] is still a reference as long as biological studies are referred to. The electron tomography has recently been more and more employed as an investigation method in the field of materials as the result of the high technological maturity of the electron microscopy techniques since the very beginning of the last century. Since soft materials and polymeric nanostructures are three-dimensional structures, electron tomography has been successfully applied in a quantitative manner at the mesoscale or with a sub-nanometric resolution as an ideal tool for their 3D characterisation. A large variety of polymeric structures such as block copolymers [5] or nanocomposite material [6] have been thus studied. From the inorganic material perspective, the teams conducted by de Jong (Utrecht University) and Midgley (Cambridge University) furnished pioneering works in the field of tomography at the nanoscale. In the early 2000s, the group of de Jong has performed for the first time a complete 3D investigation of a porous zeolite using TEM in the bright field (BF) mode [7]. More recently, even in the material field, the development and optimisation of experimental approaches based on the cryo-electron tomography have gained more and more attention [8]. By reducing the irradiation damages induced by the electron beam and thus the shrinkage effect of the analysed objects, these techniques allow for the 3D analysis of frozen-hydrated, vitrified biological materials and organic or hybrid materials with nanometric resolution [9]. In the case of hybrid organic–inorganic materials, a proper acquisition of tilt series can be performed either at low temperature on non-vitrified specimens or by using a low-dose mode for preserving the specimen structure during the total duration of the acquisition. However, as compared to the biological specimens, the method of single particle reconstruction (several digitised images of similar particles) does not seem to be appropriate for nanomaterials owing to the unicity of their geometrical and compositional characteristics.

Addressing the atomic structure of crystalline nanomaterials in three dimensions has been for long a challenge for electron tomography. While the detection performances have met the atomic resolution requirements in the latest years, probing nanoparticles under three dimensions and with atomic resolution has been possible only recently when new alignment protocols and reconstruction algorithms were developed. The very first testimony in this sense is brought forward by the work of Scott et al. [10], who proposed the mass-centre algorithm for the alignment of series resolved at the atom scale that were acquired on an Au nanoparticle having a diameter of 2 nm. The approach proposed for the volume reconstruction implies the use of a Fourier transform-based algorithm that allows for the achievement of atomic resolutions in 3D. The very same target but using different methods has been addressed to by using the combination of aberration-corrected TEM and of advanced reconstruction algorithms like simultaneous iterative reconstruction technique (SIRT), discrete algebraic reconstruction technique (DART), or the total variation minimisation (TVM) method. As we will see later, a high-level characterisation has been also achieved by combining analytical techniques as electron energy loss spectroscopy (EELS)-STEM [11, 12] and energy dispersive X-ray spectroscopy (EDS)-STEM [13] with electron tilt-series tomographic acquisitions.

6.3.2 *Various Working Modes*

Electron tomography (ET) under bright field transmission electron microscopy (BFTEM) is fast and easy to implement. Tomographic recording requires the image intensity to be characterised by a monotonic variation as a function of the signal of interest integrated along the thickness of the sample in each point. Signals of interest can be the mean density, the atomic number, the chemical nature or the plasmon resonances. This requirement is not fulfilled with crystalline materials, due to electron Bragg diffraction at specific recording angles of incidence. As a consequence, the use of BF-TEM in the field of materials has long been restricted to the study of amorphous materials at the atomic level, such as polymers or mesoporous structures [14–17].

For the 3D analysis of crystalline materials, the use of the annular dark field (ADF) imaging technique in the scanning TEM mode (STEM) constitutes an attractive alternative. For high collection angles in the ADF mode (HAADF), the contribution of Bragg-diffracted electrons diminishes strongly, and therefore, the recorded signal is predominantly incoherent, improving in this way the projection requirement for the tomography. This STEM-HAADF incoherent mode is also known as the Z-contrast 3D mode, since the contrast in the initial images depends mainly on the specimen thickness and scales with the local atomic number [18, 19]. For many situations, the 3D analytical information can indirectly be obtained through the dependence on the atomic number within the tomographic signal. However, the STEM-HAADF tomography is not efficient for materials with elements having close mean atomic numbers owing to the low contrast between them.

One of the most valuable methods to perform 3D chemical analytical mapping over a few hundred nanometres is to perform tomography in the energy-filtered TEM (EFTEM) mode [20]. This technique is one of the three different analytical techniques that can be implemented in a TEM. It is worth mentioning that the “analytical tomography” has an impressive potential since it combines the ability of conventional electron tomography to get 3D information at the nanoscale and the chemical selectivity of the EFTEM imaging. More specifically, it combines the tilt-series approach with the image acquisition in energy-filtered imaging mode. In principle, by carefully choosing the energy windows corresponding to the ionisation edges of the elements of interest, we are able to record chemically selective 2D images. This *modus operandi* is repeated for each tilt angle, and projection series of the spatial distribution of the elements are obtained in this way. They are further used to build up the 3D elemental map. Being rather difficult to operate under the tomography methodology [21, 22], this powerful method did not receive much attention in the field of material science up to now.

More recently another analytical TEM technique, EELS-SPIM tomography, has been developed [11, 12]. This technique consists of reconstructing the information extracted from EELS spectrum images (SPIM, images on which every pixel contains a full EEL spectrum, which has been recorded by scanning the electron beam at the surface of the nano-object) [23, 24] in 3D, by acquiring a series of EELS-SPIM at different tilt angles [12, 23].

Almost all electron microscopy modes that have been developed for the 2D imaging of samples can be adapted for the 3D investigation of nanomaterials. Obviously each mode—electron holography [23], EDS spectroscopy [11], EELS spectroscopy [12, 13, 23, 25], etc.—brings up its own advantages in terms of the signals acquired and the information accessed. However, adding the third dimension to the 2D imaging is not straightforward as specific requirements need to be fulfilled: large magnifications, large amounts of data to be rapidly collected and processed and new processes necessary to combine various bits of information collected on a single sample. In this context, the combination of recordings under various modes might be mandatory for the study of complex structures [23, 24].

6.3.3 Methodologies: Experiment and Calculation

From a practical point of view, electron tomography is developed in several steps: the acquisition which consists in acquiring a series of projected images by tilting the specimen with respect to the incident beam for the largest possible angular range. Afterwards, the raw images are stacked and carefully aligned, and then in a second step, the volume reconstruction is carried out. After volume rendering, data segmentation and modelling are the next steps for accessing the quantitative analyses of the investigated volumes. These steps are separately detailed in the next sections, by highlighting the role of each step, its specificities and obviously the difficulties encountered in practice.

Acquisition of a Tilt Series

The acquisition of tilt series can be carried out in any microscope equipped with a high-tilt specimen holder and data acquisition software. The latter ideally provide an automated recording of tilt series over a predefined angular range and a close control of both the defocusing and specimen drift at each tilt angle. The recorded images need to be real projections of the whole sample; in other words, the imaging depth of field must always be larger than the sample thickness. The maximum tilting angle and implicitly the number of projections do define the spatial resolution in the two directions perpendicular to the tilt axis, whereas along the tilt axis, the resolution remains the same as that of the initial 2D images. The corresponding spatial resolution/direction relationships have been detailed by Frank and McEvan [25] in their pioneering work edited in the early 1990s.

The use of an EFTEM tomography mode for obtaining reliable 3D chemical elemental mapping implies the acquisition of multiple series of images as a function of the number of elements to be explored. Basically, three energy-filtered TEM images are recorded, for each tilt angle and for each element, in addition to the zero-loss series that can be recorded twice. This methodology, e.g. known as the three-window method, allows for a proper extrapolation of the background for the

quantitative extraction of the chemical signals [26, 27]. This approach lengthens the duration of the recording sessions but offers a good assessment of the background and elemental projections. This full set of recordings is carried out for every element of interest within the specimen.

As mentioned above EELS-SPIM or EDS-SPIM tomography techniques require the acquisition, in parallel to the HAADF signal, of the corresponding spectroscopic signal. However, it is worth mentioning that these analytical tomographic techniques present the drawback of high acquisition times and therefore high-energy doses. Thus, this aspect should always be taken into account in order to limit the sample possible degradation.

HAADF-/EELS-STEM, EDS-STEM EFTEM Specificities

As previously stated, the use of the parallel beam bright field mode for the 3D analysis is not well adapted for the study of crystalline materials owing to the Bragg-diffracted electrons which make it difficult to correct the observation of the object at various tilting angles. To overcome this difficulty, the signal is improved by using the high-angle annular dark field (HAADF) detectors under scanning (STEM) mode because the recorded signal is predominantly incoherent and the projection requirement for the tomography is satisfied in this way. The acquisition of scanning TEM tilt series involves the simultaneous acquisition of a BF and DF series by using a circular centred detector for the BF and an annular detector for the HAADF. In addition, as aforementioned, STEM tilt-series acquisition allows for the simultaneous recording of other spectroscopic signals, as it is the case for EDS and EELS tomography. The focusing depth of the electron beam is commonly of the order of a few tenths of nm, which ascertains the position of the investigated nano-system to be in the focal volume. Ideally, the acquisition software automatically modifies the tilt angle of the specimen holder according to the input scheme, i.e. in Saxton or continuous modes. At the same time, a close control of the defocusing and specimen drift is automatically performed for each tilt angle. Moreover, the software developments actually allow for the automatic tuning of the beam focus for keeping the focal point onto the tilted specimen. The main advantage of simultaneously acquired BF and DF series relies on the one hand on the signal complementarity and on the other hand on the achievement of spatially correlated volumes. It is well known that in the HAADF mode, the signal intensity scales with the Z atomic number, and therefore, this methodology is well adapted to the detection of heavy elements. The nano-systems analysed by HAADF comprise both single element nanoparticles with specific geometries or complex nanostructures and nanocomposites constituted by elements with significantly different atomic numbers. Under BF-STEM, one is able to access the system porosity. The information complementarity is totally ensured as the DF, and BF volumes are spatially correlated, and a precise direct comparison of the two volumes can be successfully performed. The STEM tomography remains a technique rather difficult to perform, and lots of undesired events might occur, like the specimen contamination or beam damage during long

acquisition duration. However, this approach remains interesting not only for the investigation of crystalline materials but for the 3D exploitation of beam-sensitive materials, situations for which low-intensity currents and short exposures need to be used during the scanning step.

When the nano-systems to be analysed are constituted by elements with close atomic numbers, a possible solution for the 3D analysis is the “analytical tomography”, the EDS or EELS tomography. EDS tomography is very difficult to implement as it requires up-to-date X-ray detectors able to cover high angular solid angles that became commercially available only in the last 2–3 years, and the approach requires huge hardware resources for the data acquisition and analysis. Still in an early stage, many efforts will be most probably done for the development of the EDS methodology as an alternative to the analytical tomography. Indeed, it is important to point out that one of the main advantages of this technique is that it allows for the simultaneous detection of a large range of elements (including those with a high atomic number). The EFTEM tomography requires the recording of multiple images for each tilt angle: a zero-loss (ZL) image that filters the elastic electrons and, for each element of interest, three energy-filtered images taken nearby its ionisation edge. In practice, once the zero-loss tilt images exhibiting good signal-to-noise ratio (SNR) are properly aligned, the alignment of the elemental projections can be done by using the very same alignment parameters. As a result, spatially correlated series of projections are obtained. In analytical tomography the prior knowledge of the external morphology and porous structure of the object is particularly beneficial as it allows for the extraction of the elemental volumes considering only the voxels corresponding to the material. The last step consists in a quantitative combined analysis of the elemental volumes and will be developed in the next sections. The spatial resolution of the 3D elemental maps depends on (1) the recording parameters (pixel size, maximum tilt angle, number of projections) and the data processing (accuracy of the image alignment, algorithm used for the reconstruction) and (2) the resolution in the 2D elemental projections [28]. Roughly, this leads to a theoretical 3D resolution of about 1–2 nm. In practice, the actual resolution strongly depends on the SNR [29]. Deeper insight on the methodology developed for analytical tomography is given in the Sect. 4.4, by analysing the case of nanomaterials constituted by an intimate mixture of silica and alumina, systems largely used for industrial applications.

Principal Reconstruction Algorithms: WBP, SIRT, ART, DART and New Algorithmic Approaches

Two main routes are usually considered for the specimen reconstruction from its recorded projections. The first one relies on the fact that the recorded intensity values can be used to calculate the 3D representation of the sample reciprocal space. Basically, each projection of the sample is univocally related to a Fourier central slice orthogonal to the projection direction, and therefore, the Fourier transform of this reciprocal space uniquely yields a reconstruction of the real space of the sample. Since the reciprocal space recorded through electron tomography is made out

of non-evenly and non-periodically distributed point values, the Fourier calculations even in the fast Fourier transform (FFT) mode are complicated; it becomes more convenient to perform the reconstruction calculations in the direct space. Here, the intensity of one pixel on one projection image lays on a straight-line segment orthogonal to the image at the position of the pixel. By repeating this operation for each equivalent pixel in the full set of images and at the point where the segments intersect in space, the sum of the intensity values on each segment, one accesses the voxel that envelops this intersection in the real 3D space. This technique is named weighted back-projection [30].

The quality of the object reconstruction strongly improves when the number of recording angular steps is increased; it can be further enhanced by correcting the angular cosine dependence of the projection of the object and by varying the tilt angle of the sample according to a cosine function [31]. As the number of recorded projections is limited, the “star” artefacts occur, and consequently, the quality of the reconstructed matrix of the object is degraded [32]. In addition, the tomographic tilt series have a wedge of missing data corresponding to the angular range uncovered due to the limited value of the maximum angular rotation of the specimen holder, where no images are recorded. This TEM-specific limitation causes distortions in the 3D reconstructions. Furthermore, the spatial resolution is degraded in the direction of the incident electron beam at 0° tilt. All these artefacts can be significantly attenuated applying iterative algorithms that improve as well the signal-to-noise ratio within the reconstructed volumes. After each calculation of the reconstructed matrix, projected images are calculated and compared with the original ones. A least squares comparison technique allows reaching a stable matrix in a convergent process. The most popular algorithms are implemented in the SIRT and the algebraic reconstruction technique (ART). Their reliability and stability are discussed in Refs. [33] and [34].

The development of electron tomography for the material science research has led to the development of even more powerful reconstruction algorithms, which take advantage of the discrete nature of the reconstructed volume. The DART quotes with the association between the number of grey levels used for the reconstruction and the exact number of component known to be present in the sample under study [29].

More recently other alternative approaches based on compressive sensing (CS) or TVM have been developed [35]. The compressive sensing considers that a small number of well-chosen measurements can suffice to reconstruct signals that are amenable to sparse or compressible representation. In addition, the CS significantly reduces artefacts present in conventional electron tomography reconstruction (blurring of object boundaries, elongation, etc.) even if far fewer projections are employed.

Qualitative and Quantitative Volume Analyses

Several aspects can hamper the qualitative and quantitative interpretation and analysis of tomograms: the artefacts due to the missing wedge and to the limited number of projections, the low SNR and the low contrast between the various parts of the

analysed object. The artefacts commonly lead to volume distortions and might mask the information along the incident beam direction. The most tedious step, which can induce considerable errors in the quantification, is the data segmentation process. It consists in decomposing the tomogram into its structural components by identifying the sets of constitutive voxels. Although several automatic or semiautomatic approaches have been developed based on simple density thresholds or more sophisticated threshold approaches, manual segmentation is sometimes the most reliable approach: the user assigns the structural features using visualisation tools. Once the parts of interest have been extracted from the volume, most of the 2D image analysis processes can be easily generalised to 3D allowing one to calculate the parameters of interest, as described in the next sections by considering suggestive and representative examples.

6.4 Application to Nanomaterials and Nanostructures

The nano-science demands nowadays the continuous development of specific tools aiming at first exploring and then controlling the materials structures, morphologies and chemistry and their subsequent properties at the atomic level. As a function of the applications envisioned, one assists at the building up of more and more complex three-dimensional nanostructures and nano-architectures with complex morphologies that dictate their specific responses. In the catalysis field, for instance, the active phase localisation, accessibility and the surface-active area are parameters of huge impact for the catalytic activity. Exploring the morphology and chemistry of complex systems would most probably open new routes for understanding their behaviour under operational conditions. Another example concerns the metal nanoparticles widely used in the fields of photonics, optoelectronics, photocatalysis and bio-sensing applications. Their optical response is dominated by the localised surface plasmon resonances (SPRs), whose spatial distribution strongly depends on the NP morphology [36–40]. The correlation between the morphology and the properties of complex nanostructures is a key issue for the comprehension of their characteristics. Electron tomography will furnish valuable information on the 3D characteristics of structured nanomaterials with the nanometre resolution.

6.4.1 *Morphological Analyses of Nanostructures and Nano-objects*

In the following section, we will illustrate the quality of the information gained when using electron tomography as well as the technique applicability to various types of nanomaterials and nano-objects.

Tailoring Few Layer Graphene Structures by Fe-Based NPs

Controlling the size of graphene nano-sheets and nano-ribbons has presently become a hot topic in the field of material science. Owing to their outstanding physical and chemical properties, graphene nano-ribbons with well-defined dimensions are ideal candidates for the production of nanocomposites that can find applications in many fields such as energy storage, electronics, catalysis, etc. The production of graphene nano-ribbons with a well-defined geometry remains a technological challenge, and in this sense, several routes have been considered: the mechanical and/or chemical exfoliation of graphite [41, 42] and subsequent selection of nano-ribbons as a function of their size and thickness, the catalytic unzipping of carbon nanotubes (CNTs) [43] or a combined approach.

In principle, under well-controlled atmosphere, a supported active nanoparticle does react with its support, and as a result, the system morphology changes drastically. When Fe-based NPs are deposited onto carbon-based supports, one assists to significant changes of the support morphology as, for instance, from CNT to GNR or the creation of trenches on the surface of few layer graphene (FLG) supports. A complete investigation of the morphology changes as induced by the catalytic cutting of FLG sheets has been carried out by electron tomography [44]. Initially the Fe-oxide NPs locate on both sides of the supports at the FLG steps and edges with different heights or on the terraces (Fig. 6.2a). After thermal treatment under

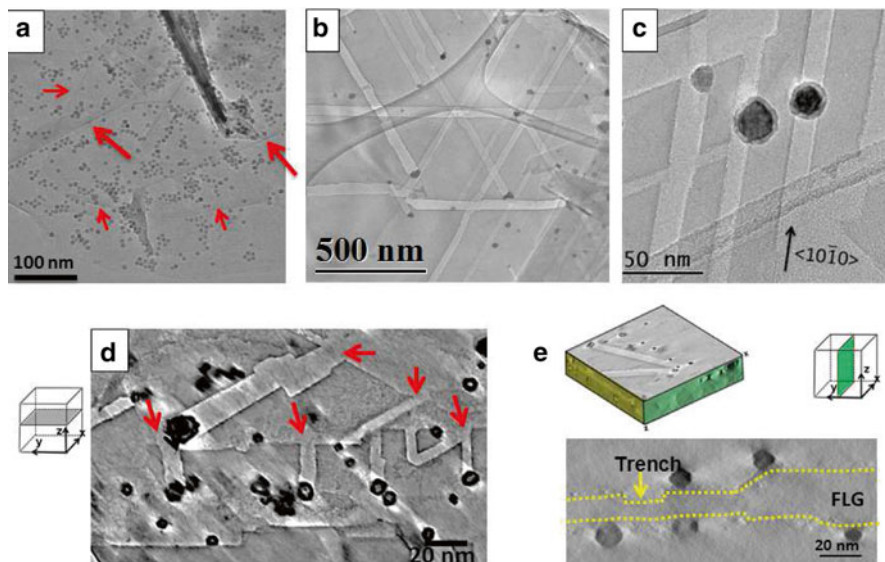


Fig. 6.2 Global view of the nanostructured few layer graphene. 2D TEM micrographs of typical Fe-based NPOs onto FLG (a) before and (b) after catalytic cutting accompanied by (c) the change of NP morphology. 3D overview of the cut system with (d) the arrows pointing to the initial location of NPs (xy slice) and (e) the volume representation showing roughly the system topography. Reprinted from Melinte et al. [44]

hydrogen flow, the NPs dig the surface of the supports forming trenches on its surface (Fig. 6.2b) along well-defined crystallographic directions (Fig. 6.2c). The NP morphology changes from homogenous to core-shell or hollow structures, accompanied by a change of the NP chemical composition (see in more detail supplementary information in ref. [44]).

From a statistical analysis, it has been shown that the only NPs located initially at the FLG steps and/or edges can cut trenches and that the cutting activity of Fe NPs is significantly higher than that of Fe_3O_4 or Fe-rich regions exist on the cutting front direction. From a 2D analysis, using different contrasts, one identifies the presence of sharp superimposed long morphological features within the support with possible various thicknesses. Their exact depth and location can be explored only by means of 3D imaging. Indeed, ET identified the presence of NPs and trenches on both sides of the FLG support. The role of FLG topography on the cutting phenomenon is also identified. During its motion, a cutting NP can encounter support defects, such as steps and edges. If the NP crosses a step-up defect with the height smaller than its diameter, the NP continues its path by creating a trench (Fig. 6.3a), whereas when the step-height is higher than the NP diameter, the NP digs a tunnel (Fig. 6.3b) in the same direction as before it encountered the step. It is however interesting that for both situations, the basal plane of the trench or channel remains flat and constant. When the NP meets a step-down defect, it either stops or changes its moving direction; see Fig. 6.3c, d, respectively. With all these elements, we are free now to turn our attention to the synthesis of graphene nano-ribbons, by considering a chemical exfoliation procedure as the one described by Ihiwakrim et al. [45] for isolating individual features with well-defined geometries and thicknesses.

Porosity of Mesoporous Hollow-Shell Mixed Oxide Nanoparticles

Silica-based meso-structured nano-systems, used as drug delivery agents, have been largely investigated during the last years. They allow a high flexibility of integration of multiple properties needed for efficient imaging diagnosis and/or therapeutic treatments. Lots of efforts have been spent in designing new silica-based nano-carriers with mesoporous architecture able to carry and release progressively important amount of drugs [46, 47]. One of the strategies consisted in doping the silica matrix with a few percent of zirconium. This methodology allows a very good dispersion and co-condensation of zirconium atoms within the silica network, producing spherical nanoparticles with meso-structured core and a dense shell. The zirconium-oxide surfaces are expected to catalyse the fast condensation of silicate species directly onto the cargo, and this would in principle promote a progressive rearrangement of both the meso-structured core and the shell. The raised questions focused on the pore connectivity within both the core and the shell and whether the shell is uniform and continuous around the core, or we deal with the presence of pores that would provide high accessibility to the nano-carrier. Since the BET experiments furnished no conclusive information on the pore connectivity and core accessibility, a very precise 3D morphological investigation of the cargo after drug

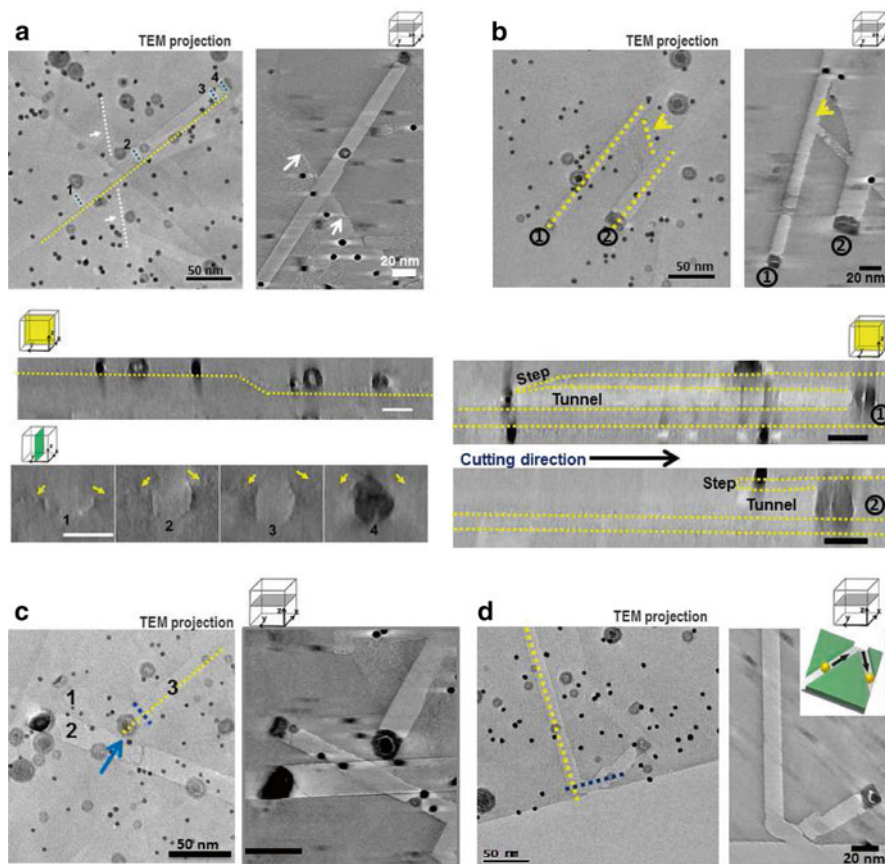


Fig. 6.3 The role of support tomography on the cutting process. 2D projections and slices redrawn from the reconstructed volume showing the impact of step-up and step-down defects encountered by the NPs. As a result, the NPs encountering a step-up defect (a) create trenches with the walls geometry defined by the NP shape when the step-height is less than the NP diameter and (b) dig tunnels within the support when the step-height is larger than the NP size. At the intersection with a step-down defect, the NPs either (c) stop or (d) change their cutting direction. Reprinted from Melinte et al. [44]

release was needed, by means of electron microscopy. Firstly, one emphasises the porous structure, and secondly, one concentrates on the zirconia location within the porous core.

As anticipated by the 2D analysis, interconnected meso-pores with irregular shapes and mean diameters of 8 nm do cross the silica core, whereas the shell appears to be a “continuous” coating with homogenous thickness. It is however marked by the presence of micro-pores with sub-nanometre size that go across the shell’s complete thickness. In the STEM HAADF mode, the intensity scales with the Z atomic number and therefore one may associate the highest intensity with the

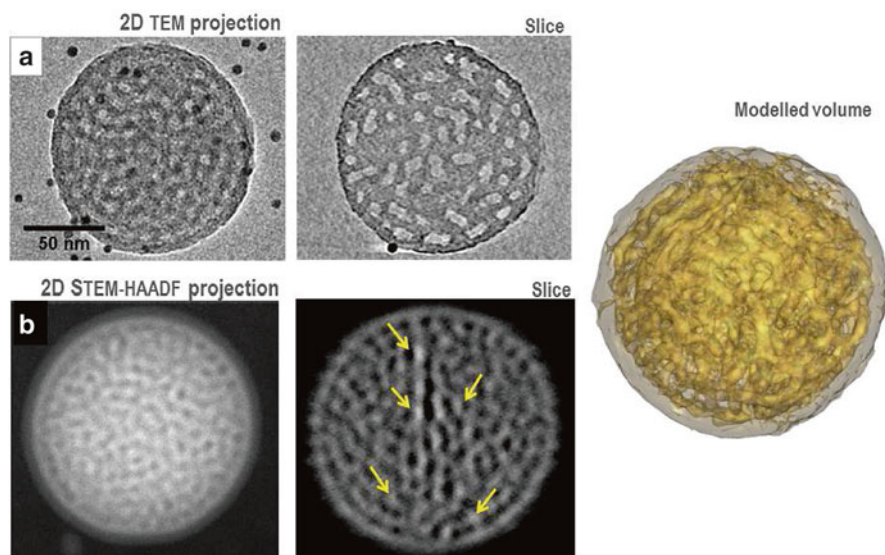


Fig. 6.4 Electron tomography of a silica structure embedded into a denser Zr-enriched silica layer. (a) The homogenous distribution of the mesoporous volume is marked by (b) the presence of Zr-rich areas within the meso-pore rims (*arrows*). (c) Volume modelling allowing for the achievement of valuable 3D quantitative information. Reprinted from et al. [to be published]

presence of Zr. It is surprising though that it can be identified not only within the shell but also within the core-silica as well into silica-meso-pore rims (arrows in Fig. 6.4b). Even if ET remains a local technique of investigation, one of its advantages is to give access to quantitative parameters. In our case, the analysis of several volumes showed that 40 % of the volume is porous, whereas the specific surface is six times larger than the external surface of the volume.

Au and Au/Ag Nano-bipyramids: Shape and Plasmon Response

Owing to their optical properties, the structure and morphology of noble metal-based nanoparticles with homogeneous or core-shell structures have been widely explored, for their optical response depends strongly on their shape and surface topography. Let us consider the case of core-shell Au–Ag bipyramids (BP). By exploring for the first time the Z-contrast within the STEM-HAADF tomography, it was possible to identify the bipyramidal shape of these nanoparticles constituted by a homogenous core embedded in an Ag matrix with a thickness of several nm. Secondly, we have identified and quantified the shape and structural defects within the NPs: transverse atomic steps perpendicular to the bipyramid long axis about everywhere on the particle surface (see the model in Fig. 6.5). The main advantage of this approach is its reliability for quantitative exploitation, which allows one to assess the inhomogeneous

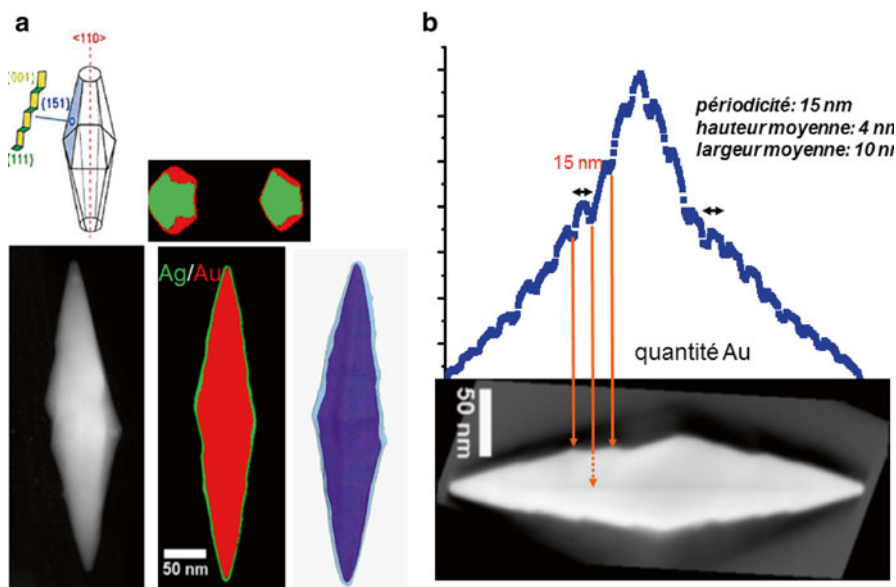


Fig. 6.5 Electron tomography (STEM-HAADF) of an Au–Ag core-shell bipyramid. (a) The distribution of Ag shell on the surface of Au nano-bipyramid filling the surface defects of the Au core. (b) Representation of the Au amount as assigned from a numerical cut within the volume

character of the steps occurrence. It is important to mention here that the proper quantification of the steps requires a perfect alignment of the BP, e.g. along its long axis. Even so, no complete access to all steps is ensured due to the random orientation of the steps against the BP long axis. From a quantitative perspective, performing a numerical cutting operation within the volume and subsequent calculation of the Au amount for each slice can search a solution. Since the variation of the Au amount along the axis exhibits a singularity at the location of a step, this type of representation identified the steps characteristics of mean periodicity, width and height, as being 15 nm, 10 nm and 4 nm, respectively. From a fundamental point of view, the presence of steps on the NP surface can strongly modify its optical responses as such defects act as hotspots, with a high concentration on the electric field lines [48].

CoPt Nanoparticle Grown on a NaCl Substrate

The 3D morphology of particles always has a huge impact on their physical and chemical characteristics. Therefore, the strict control of the particles' size, shape and crystallography has become a real challenge in the field of catalysts. Whilst the surface's energies properly describe the shape of macroscopic particles, in the case of NPs, many other structures as edges, vortices, surface state and atomic relaxation derive from the atoms disposed in small clusters [49]. From a statistical viewpoint, the NP faceting, shapes and morphologies vary significantly and differ from the

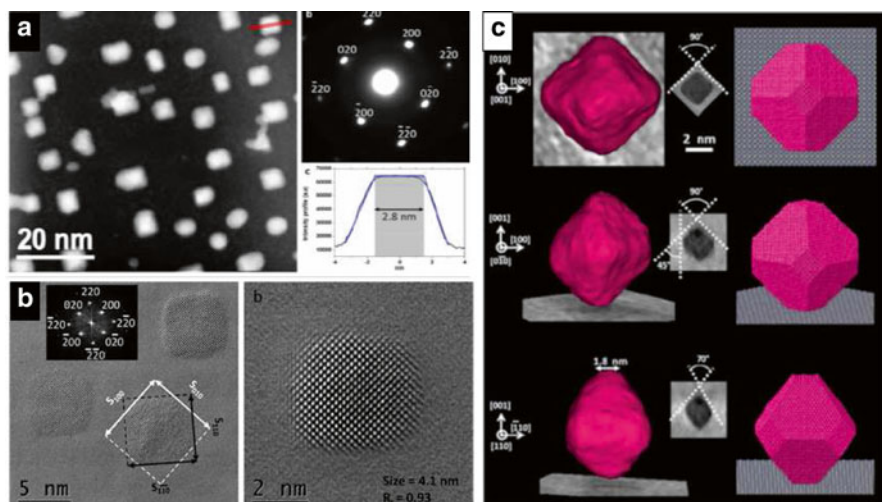


Fig. 6.6 Distribution and shape of chemically disordered CoPt NPs epitaxially grown onto NaCl substrate. (a) NPs' homogenous distribution after transfer on a carbon membrane. (b) HR images of NPs exhibiting $\langle 110 \rangle$ edges and truncated facets along the (100) and (010) directions. (c) Volume truncations as explored by STEM-HAADF electron tomography and molecular dynamics simulations (after system relaxation) along the [001], [0-10] and [110] directions (from *top* to *bottom*). Reprinted from Florea et al. [22]

energetically stable nanostructures even when the synthesis parameters are closely controlled. This is mainly due to the synthesis kinetics and to the NPs interaction with their environment. All these aspects have been checked with monometallic NPs [22]. Adding a second component introduces a new source of instability. Let us consider an intensively studied bimetallic system: CoPt NPs. These NPs have been epitaxially grown onto a NaCl substrate and subsequently investigated by HR-TEM, STEM and electron tomography, and the results were checked through molecular dynamics calculations (Fig. 6.6).

Slightly different-sized CoPt NPs exhibit high faceting within the chemically disordered FCC structure. The NPs are truncated octahedrons with different truncation ratios as a function of the NP size, in a way such that the larger the particle, the rounder its shape. In addition, up-down symmetry has been identified for all NPs, no matter their size. More specifically, the (001) support-interface facet is similar to the (001) vacuum facet, suggesting a negligible contribution of the fcc-CoPt/NaCl adhesion energy to the interface energy.

6.4.2 3D Distribution of Nanoparticles on Supports

The 3D distribution of NPs on supports and their behaviour under well-defined conditions are key issues for material implementation in applications. For example, the attrition of electron transport properties of semiconductive nanowires grown by

chemical vapour deposition is mainly attributed to the presence of residual NPs on their surface (see Sect. 4.3.2), or in catalysis, the catalytic activity is closely related to the spatial and chemical distribution of the active phase, etc. During these working processes, the materials are submitted to more or less extreme conditions, such as high temperatures/pressures, gas flows or high electric fields. In this context, controlling the size, dispersion and shape of nanoparticles (NPs) in the high-temperature range and under specific conditions is a key topic for the development of new technologies. This section highlights the potential of electron tomography as combined with the in situ TEM, high-resolution imaging and spectroscopy for assessing the behaviour of complex nano-systems.

Co-Based Nanoparticles (NPs) Confined by CNTs

The confinement of magnetic Co-based NPs by inert and stable matrixes such as CNTs can be considered as an appropriate solution against NPs oxidation and therefore for the conservation of their magnetic and/or catalytic properties. Co-based NPs with mean sizes of 50 nm were casted inside multiwall CNTs by solvothermal synthesis, generating nano-peapod-like nanostructures. They exhibit specific morphologies marked by the NP faceting and the presence of voids and pseudo-fractures, i.e. closed fractures oriented along well-defined crystallographic directions within the same CoO monocrystalline grain [50]. The oxygen concentration in one NP is inhomogeneous, such that the oxygen concentration appears to be higher at the NP edges and the pseudo-fracture rims. For the initial system, the lengths of the pseudo-cracks are inferior to the grain dimensions, and their disposal is predominantly radial being surrounded by randomly disposed voids.

The hydrogen-assisted thermal treatment leads to the opening of the pseudo-fractures, as shown schematically in Fig. 6.7d, e. It is however interesting to note that the pseudo-fractures are practically confined within the same mono-crystal for the initial oxidised Co NPs, whereas after reduction one observes fracture opening, but the grain geometry is roughly confined due to NP encapsulation. The behaviour of such structures in the high-temperature range can furnish insights on the most probable morphology changes under operational conditions. The in situ thermal treatment identified a temperature two times higher necessary for the change of NP shape and subsequent coalescence in the case of reduced system as compared with the as-prepared specimen.

Au Nanoparticles (NPs) on Silicon Nanowires (NWs)

Semiconducting silicon nanowires (NWs) synthesised by chemical vapour deposition are promising candidates for building up complex structures such as biosensors or programmable nanowire circuits. One of the most employed methods for their synthesis is the vapour–liquid–solid (VLS) growth technique. This method very often implies the use of Au as catalyst and leads to the production of NWs with the

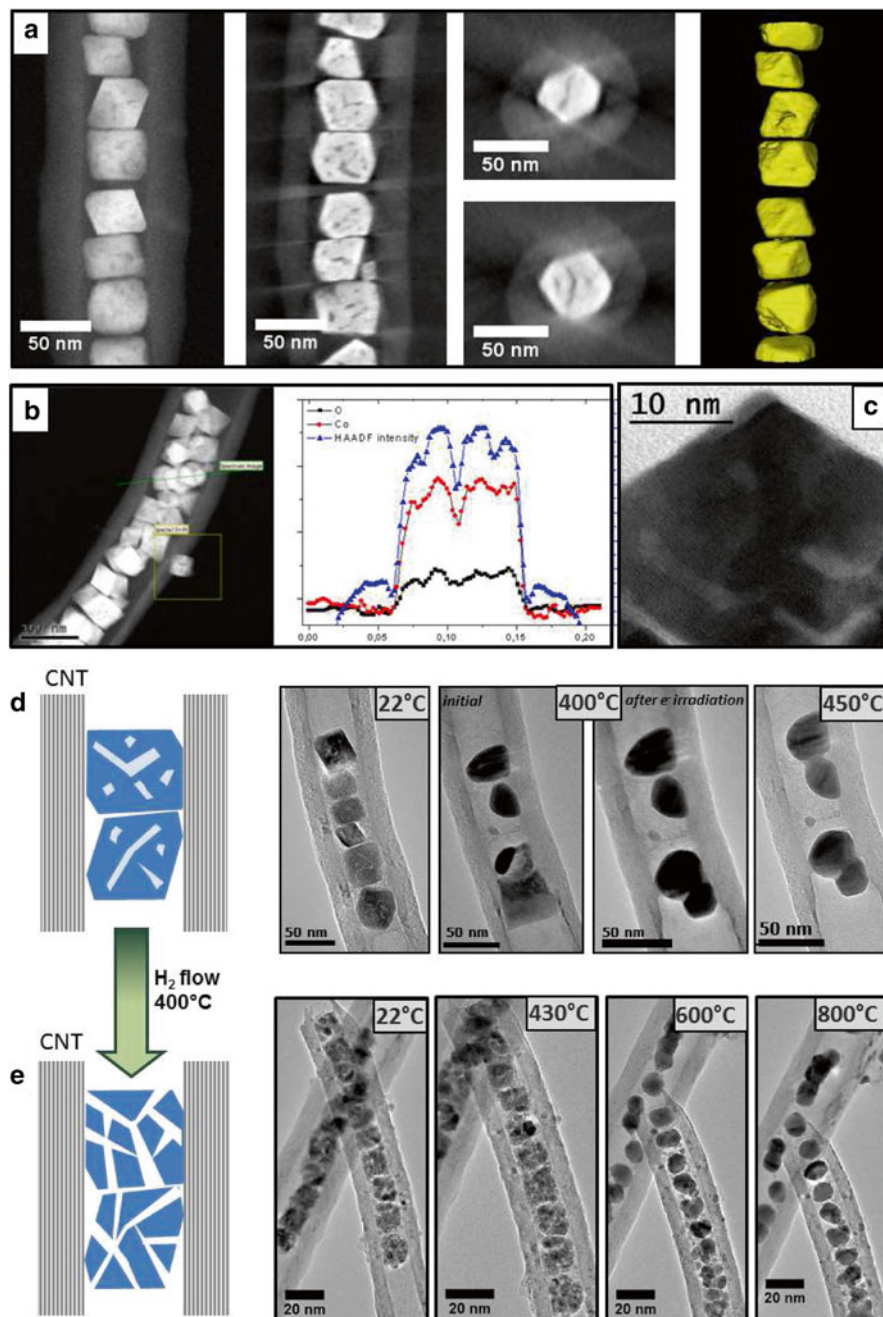


Fig. 6.7 Morphology and annealing behaviour of Co-based NPs casted in carbon nanotubes. Monocrystalline faceted Co-based NPs (a) randomly distributed within the tubes exhibit inner voids and pseudo-fractures that (c) do not cross the NPs. (b) The NPs' outer surface as well as the voids and the pseudo-fractures' rims are rich in oxygen. The hydrogen-assisted reduction leads to crack opening. The porous defects within the nonreduced and reduced Co NPs disappear through thermal annealing at (d) 400 °C and (e) from 600 °C, respectively. Reprinted from Baaziz et al. [50]

surface contaminated by the presence of Au residuals. These residues have a key role on the transport properties of NWs, an issue that is not completely covered up to now. Parameters like residues' size and their scattering on the nanowire's surface are obviously of huge importance. The measure of the transport properties carried out by AFM tip work function has revealed the strong interplay between Schottky interface junctions, surface conduction along the Au-rich nanowire sidewalls and intrinsic conduction of the NW. In order to get a deeper insight on the role on the transport properties of Au on the sidewalls, the question of system morphology needs to be addressed [40]. Indeed, spherical Au NPs with mean diameter of 2 nm are uniformly distributed on the NW surface, and they coalesce when heated at 750 °C. It is highly interesting to note that a longer duration of the thermal treatment leads to the formation of a thin layer. This layer grows along the NWs' length, whereas the NW end changes completely the morphology in a club-like structure. Certainly, questions like the presence of a pure Au coating or of the AuSi alloy remain opened. However, this particular thermally induced behaviour cannot be neglected as it is equivalent to the Joule effect that takes place upon application of an intense electric field, inducing a subsequent attrition of the transport properties of the system (Fig. 6.8).

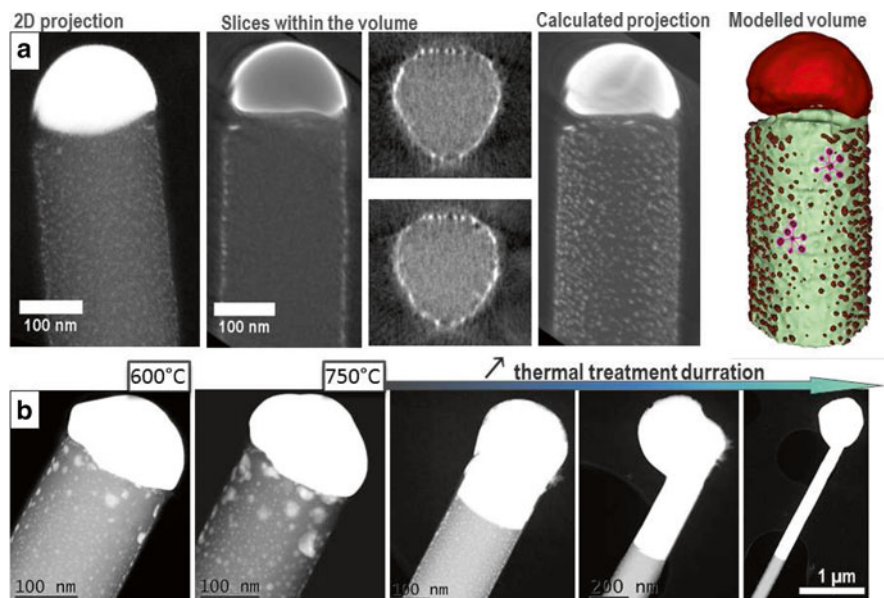


Fig. 6.8 Morphology and thermally induced evolution of Au/Si nanowires. (a) Au catalyst NPs are uniformly distributed on the outer surface of the Si nanowires, whereas a big catalyst particle sticks to the Si NW end. The surface NPs coalesce (b) at 600 °C, such that at 750 °C the Au from the tip melts, embedding the wire and completely changing the system morphology

Pt Nanoparticles (NPs) onto FLG

The perspective of using graphene as a support for Pt nanoparticles with enhanced catalytic activity is very attractive, opening a new way in the development of durable and efficient proton exchange membranes (PEM) for fuel cells. Since the major part of the catalytic reactions takes place in the high-temperature range, the stability of Pt NPs onto FLG supports is a key issue for the applications. If one considers a system made of Pt NPs with mean diameters of 2 nm, the in situ TEM approach revealed that upon heating the size distribution of the Pt NPs shifts towards two maxima centred at 3.5 and 5.5 nm [51]. In addition, questions on Pt NP faceting and sintering by coalescence and/or Ostwald ripening were addressed by considering the interaction with the FLG support (Fig. 6.9).

The NP/support interaction is the parameter controlling the behaviour of the system in the high-temperature range. This parameter strongly depends on the support topography, which is marked by the presence of edges, steps, and terraces, as shown in Fig. 6.10. Since the FLG edges and steps are marked by the presence of dangling bonds, the NPs have a strong tendency to fix there rather than onto the terraces. This latter configuration requires the presence of defect within the FLG sheet, which can be seen as traps for the metallic atoms and/or NPs. Upon heating, the NPs and atoms diffuse and coalesce being located exclusively on the steps and edges. Those from the terraces moved from the FLG surface towards the steps. From a phenomenological point of view, one assists most probably at the defect reconstruction within the FLG surface upon heating, leading to metal NPs and/or atoms dislodging and subsequent diffusion on the surface. When their diffusion paths intersect an obstacle

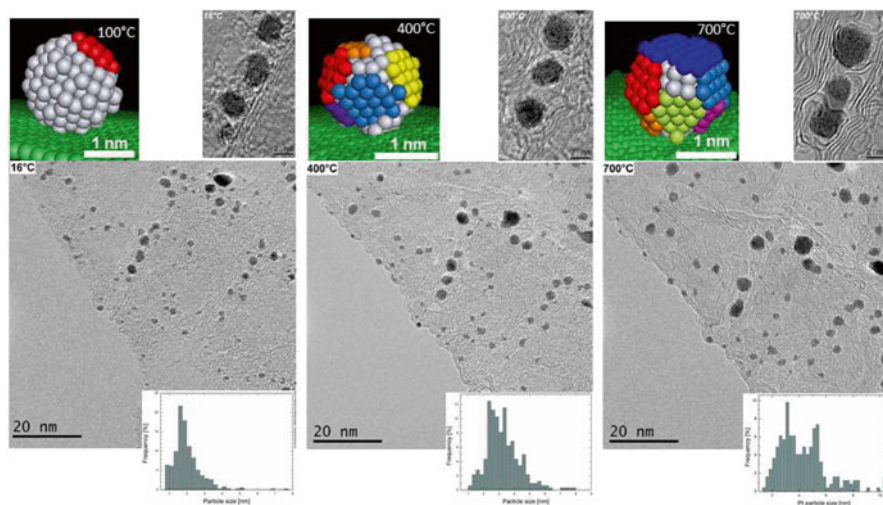


Fig. 6.9 Thermal evolution of Pt NPs deposited onto few layer graphene supports. Pt NPs with mean size of 2 nm coalesce under the impact of thermal constraints leading to NP faceting and subsequent NP size increasing. Reprinted from Moldovan et al. [51]

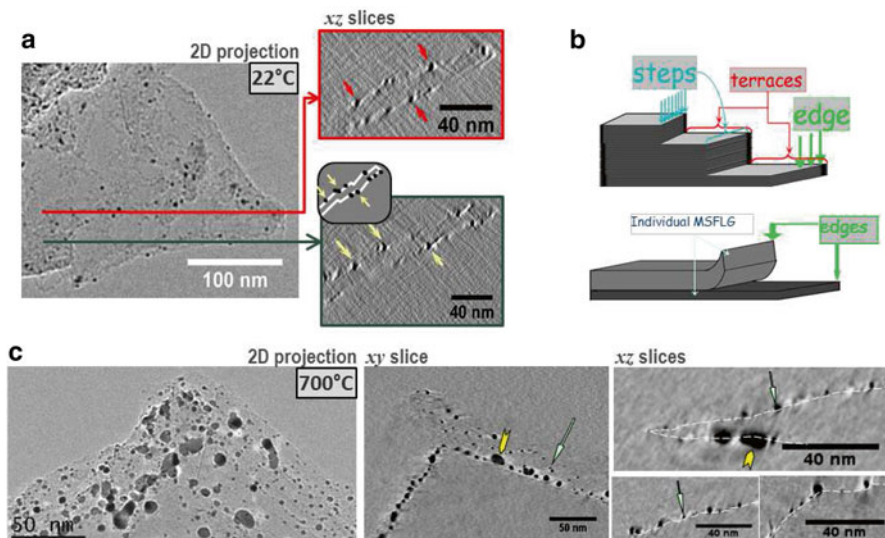


Fig. 6.10 Three-dimensional investigation of Pt NPs onto FLG supports (a) prior and (c) after in situ thermal treatment. Initially, (a) the Pt NPs and atomic clusters locate preferentially at the supports' steps and edges as well as on the terraces for typical support configurations schematised in (b). After thermal treatment (c), the NPs locate exclusively at the steps and edges. Reprinted from Moldovan et al. [51]

such as a step or an edge, they stop, and if more thermal energy is furnished to the system, they diffuse along the steps and then coalesce with other NPs placed on their path. The information gained by the electron tomography experiments allowed one to access the topography of the FLG support by bringing together the elements missing for the comprehension of the 3D structure of metallic NPs deposited on the FLG supports.

6.4.3 Long-Range Ordering of Core-Shell Co-Pt NPs

Understanding magnetisation dynamics of nanostructures is an important topic in nano-science as it opens potential new routes for various applications in optics, data storage, nano-electronics or biology. The Co-Pt-based nanoparticles have well-known magnetic properties. If they are gathered in compact assemblies or they are simply compressed into pellets, apart from their crystallography, structure and morphology, the NP spatial arrangement is expected to impact their magnetic response. After electron tomography analysis, the positions of each NP in a pellet allowed one to determine their arrangement. The distance distribution between pairs of NPs show a short-range order, with the distances of the first-, second- and third-range neighbours of 6.5, 11.5 and 16 nm, respectively.

Super-paramagnetic Co-Pt nanoparticles assembled into pellets change their spatial arrangement through mild laser annealing, such that a local super crystalline order appears at the surface of the pellet within a penetration depth of about 20 nm for a 400 nm laser wavelength [52]. Therefore, the approach of in situ heating has been carried out in order to establish the changes induced during annealing. Indeed, the NP morphology changes drastically from core-shell into a homogenous structure, whereas in terms of structure, the initial structure consisting a Co 5 nm core surrounded by a 2 nm thick Pt layer changes into a crystalline CoPt phase (see Fig. 6.11c).

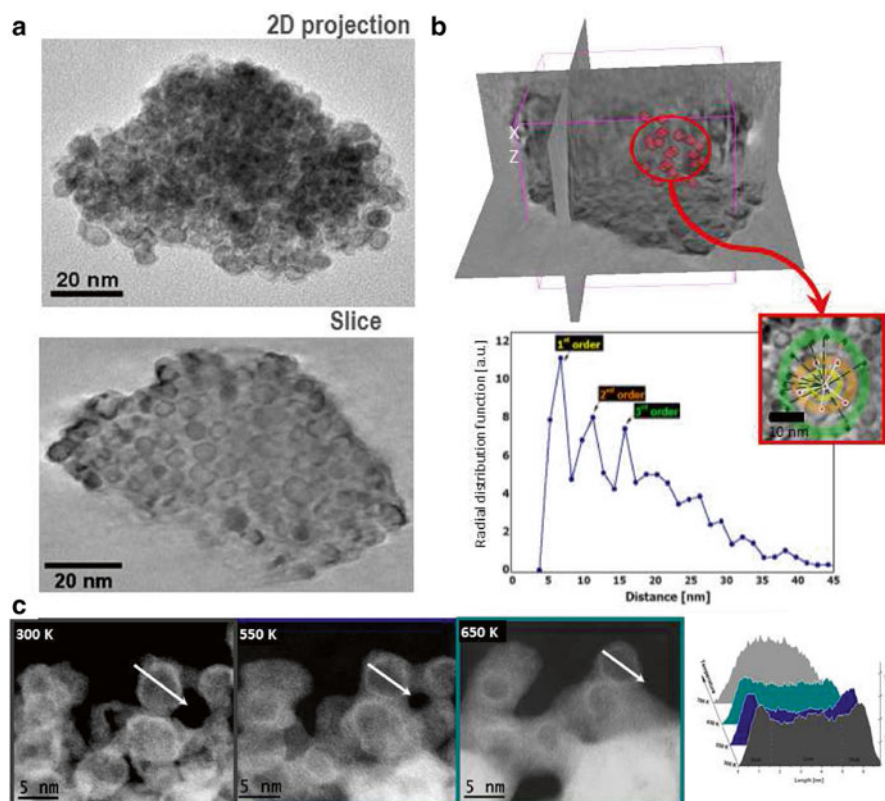


Fig. 6.11 Combined electron tomography and in situ thermal treatment study of CoPt core-shell pellets. (a) Two-dimensional projection and slices redrawn from the reconstructed volume that has been used to calculate (b) the radial distribution of NPs as function of the distances between the NPs in the pellet. (c) The evolution from a core-shell morphology towards homogenous structures as induced by the in situ thermal treatment. Reprinted from Bigot et al. [52]

6.4.4 3D Chemical Composition: Analytical Spectroscopic Tomography

EFTEM Tomography for the Study of Silica/Alumina Industrial Catalysers

Analytical tomography combines chemical mapping through EFTEM with electron tomography showing the route to 3D chemical selectivity. The experimental set-up is heavy to develop as it implies on the one hand the use of adapted materials, i.e. resistant to beam damage, and the close control of the experimental set-up itself on the other hand. This implies the prior knowledge of the specimen chemistry, which needs to be explored by EELS in order to properly define and select the corresponding energy windows. Afterwards, the acquisition, reconstruction and visualisation/quantification steps are very delicate to carry out as the signal-to-noise ratio is rather low for this kind of working mode.

We will consider as an example the case of a heterogeneous industrial catalyser made out of a mixture of silica and alumina. This kind of support is often used in the oil industry as the mix-up of the two phases generates Al–O–Si surface chemical bonds generally associated with increased acidic sites. In this way, the analytical tomography experiment has been considered for assessing the spatial distribution of Si and Al within the volume, emphasising the exploration of the surface concentration of the two elements. Figure 6.12a, b displays the zero-loss micrograph and the corresponding energy loss spectra acquired at 0° tilting. The windows marked by W1, W2 and W2 and W5 were chosen for the background extraction of the Al and Si signal, respectively. The windows W3 and W6 were used for the calculation of the signal by using the $L_{3,2}$ lines of the Al and Si. The corresponding micrographs are shown in Fig. 6.12c, together with the images after image filtering (on the right side). Once the images are acquired at each tilt angle, one obtains three series of projections corresponding to the mean mass density and Al and Si signals, which are used to calculate the three spatially correlated corresponding volumes [21]. Afterwards, one can differentiate the elements from every volume and then superimpose them to reach the “relative” chemical volume. By comparing the intensities of the elemental volumes, one can split the volume into two contributions from the Al and Si, generating in this manner an analytical model of the volume. Finally, a quantitative analysis of the volumes has been carried out. It identified that among the 50 % of silica contained in a grain, 30 % is located on the grain surface in the case of a sample prepared by liquid–solid mixture [21], as shown in Fig. 6.13a. For the materials prepared by mechanical mixture, one identifies a core-shell-like morphology with the alumina surrounding the silica core and only 15 % of silica on the grains surface; see Fig. 6.13b. Although this kind of analysis is pretentious in terms of time and resources demanded, it remains one of the most convenient resolutions for the assessment of chemical composition of nanostructures made out of elements with close Z in a three-dimensional structure at the nanometre scale.

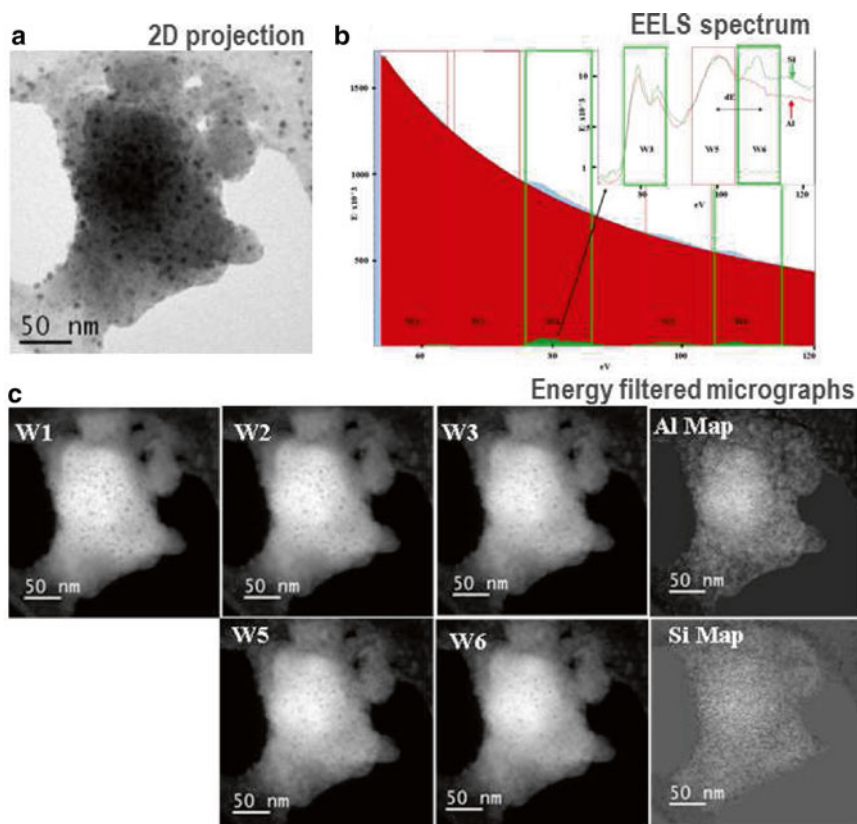


Fig. 6.12 Illustration of the acquisition series in analytical tomography; if two elements are searched for, a complete series comprises three image series, spatially correlated: (a) the zero-loss image series, which offers a high-quality contrast, and the filtered image series corresponding to the two elements. The latter are acquired by fixing the energy windows in (b) the corresponding EELS spectra and by (c) recording three micrographs for each element of interest and using the well-known three-window method. Reprinted from Roiban et al. [21]

EELS-STEM Tomography: Application to $\text{Fe}_x\text{Co}_{(3-x)}\text{O}_4@ \text{Co}_3\text{O}_4$ Mesoporous Materials

In this work the feasibility of EEL spectroscopic tomography at low voltages (80 kV) and short acquisition times was probed. This was made possible by the recent advances in TEM and the use of multivariate analysis (MVA), which were applied to mesoporous antiferromagnetic Co_3O_4 nanocast replicas of SiO_2 KIT-6 templates filled with $\text{Fe}_x\text{Co}_{(3-x)}\text{O}_4\text{Co}_3\text{O}_4$. It is worth mentioning that mesoporous silica have recently attracted much interest as hard templates for nanostructures, as the size and shape of the pores can be tailored by the choice of surfactants and synthesis paths.

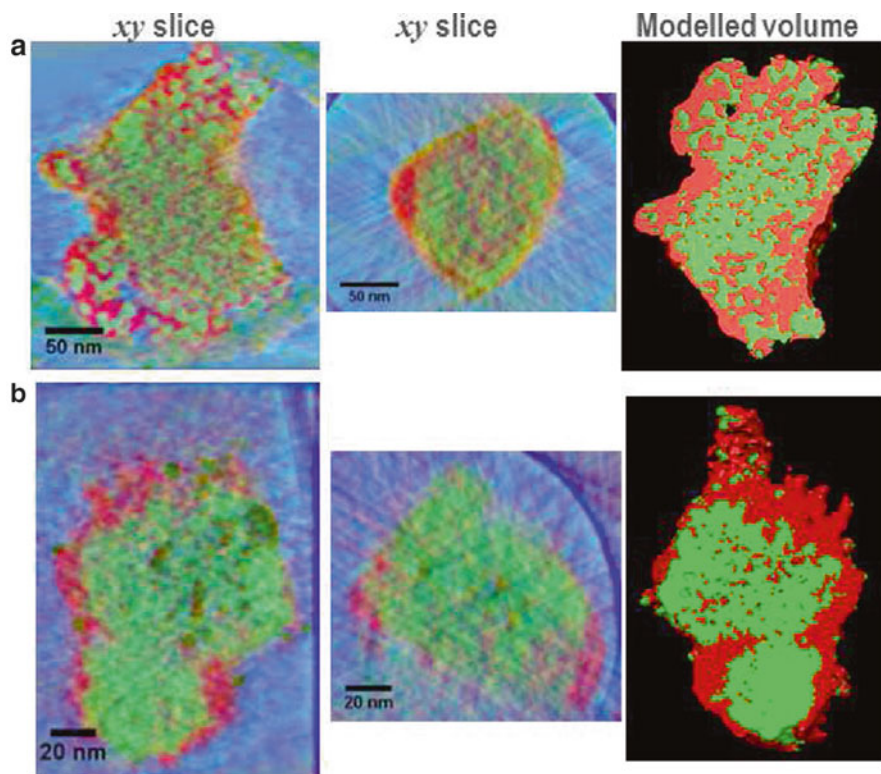


Fig. 6.13 3D analytical study of the Si (*green*) and Al (*red*) distribution within industrial catalysts made out of a mixture of silica and alumina. The Si/Al distribution (**a**) is rather homogenous for a specimen prepared through a liquid–solid mixture, whereas a silica–alumina core-shell-like structure is identified for a sample prepared through mechanical mixture. Reprinted from Roiban et al. [21]

Data acquisition was carried out on a probe C_s -corrected FEI Titan operated at an 80 kV acceleration voltage. The whole data set consisted of 48 SPIM ranging from 68.99° to -64.74° following a Saxton scheme angle step with 55×55 spectra each, acquired during 0.1 s. High-angle annular dark field (HAADF) signal was simultaneously recorded. For data treatment, MVA methods were applied, namely, the principal component analysis (PCA) and the independent component analysis (ICA) [53]. From the noisy raw spectra, enhanced O_K , Fe ($L_{3,2}$) and Co ($L_{3,2}$) edges were retrieved after PCA analysis (Fig. 6.14).

ICA successfully retrieved the Fe-oxide and Co-oxide signals of the sample as well as the background signal before the oxygen K edge (Fig. 6.15). Structural and chemical information has been obtained from the reconstruction of these signals (Fig. 6.15). Concerning the chemical information, an interesting result was revealed: the comparison between iron and cobalt signals showed that some of the iron which was intended to penetrate the structure remained on the outer surface (Fig. 6.15), whilst the rest of the iron content is uniformly distributed inside the particle.

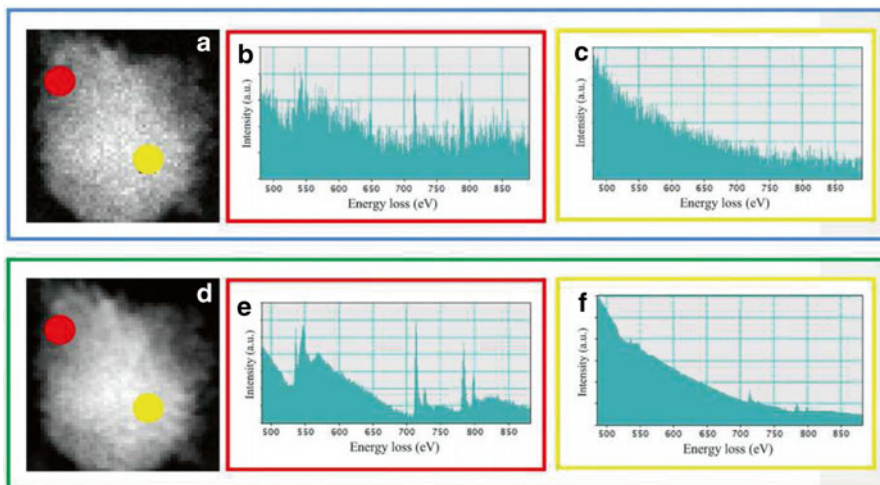


Fig. 6.14 (a, d) Spectrum images at 68.99° before (framed in *blue*) and after (framed in *green*) PCA-assisted noise reduction. Individual spectra from the edge of the particle [(b) and (e), in *red*] and the thicker part [(c) and (f), in *yellow*] are shown. Adapted from Yedra et al. [12]

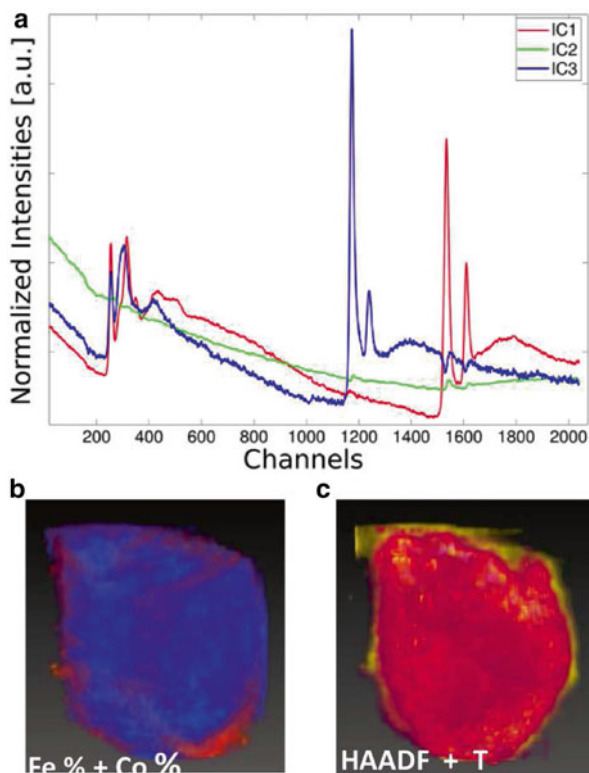


Fig. 6.15 (a) Independent components used for the reconstruction. (b) Superposition of the vortex with the Co (*blue*) and Fe (*orange*) signals as obtained from quantification. (c) Superposition of the vortex with the HAADF signal (*yellow*) and the corresponding thickness maps from ICA (*violet*). Adapted from Yedra et al. [12]

The particles are richer in iron at the edge, and therefore, iron-related chemical signals give a sharp interface between the particle and the background, where HAADF signal is very low and has fallen to background levels due to the small thickness of the sample. These results show that iron signals more precisely reconstruct the edge of the particles than HAADF. On the other hand, the thickness signal has the drawback of underestimating the border more than the HAADF signal (Fig. 6.15). However, the most interesting feature of this signal is that it is insensitive to the chemistry of the sample and independent of multiple scattering, a characteristic not found in any other signal used for electron tomography.

To sum up, EELS-STEM tomography is shown to be able to reconstruct chemical information of a sample in the three spatial dimensions.

6.4.5 Morphology of Sensitive Materials: Cryo-electron Low-Dose Tomography of Phospholipids-Silica Nanocapsules

Owing to the mild conditions required (low temperatures and pressures), the multi-enzyme cascade catalysis is an attractive alternative to chemical catalysis for the production of fine chemicals and to carry out specific reactions. For instance, the use of encapsulated enzymatic systems into silica nanoparticles has been proven to be efficient for the generation of in situ H_2O_2 and for the oxidation of polycyclic aromatic hydrocarbon pollutants in water using O_2 as oxidant (ref. [54] and reference therein). The proof of concept for the encapsulation of polyenzymatic systems in inorganic matrices and its increased efficiency for several reactions has been verified for the last 15 years. However, no direct observation by using microscopy tools has been performed because such systems are very sensitive under the impact of all kinds of radiation.

In electron microscopy, these systems exhibit important electron beam-induced damage similar to the situation of biologic specimens. Performing EM observations on such systems is not straightforward as one needs nanometre resolution within a tomography set-up for treating a complex 3D system and the system is highly sensitive to beam damage. Therefore, the approach considered combines the cryo-TEM and the low-dose electron tomography. A careful analysis of the reconstructed volume has confirmed the presence of nanocapsules with a mean size of 25 nm, made of silica cases with shell thickness of the order of 2–5 nm embedding the polyenzymes. Their shape is rounded and generally the silica shells are continuous, only a few nanocapsules exhibiting opened shells with horseshoe-like shapes (Fig. 6.16).

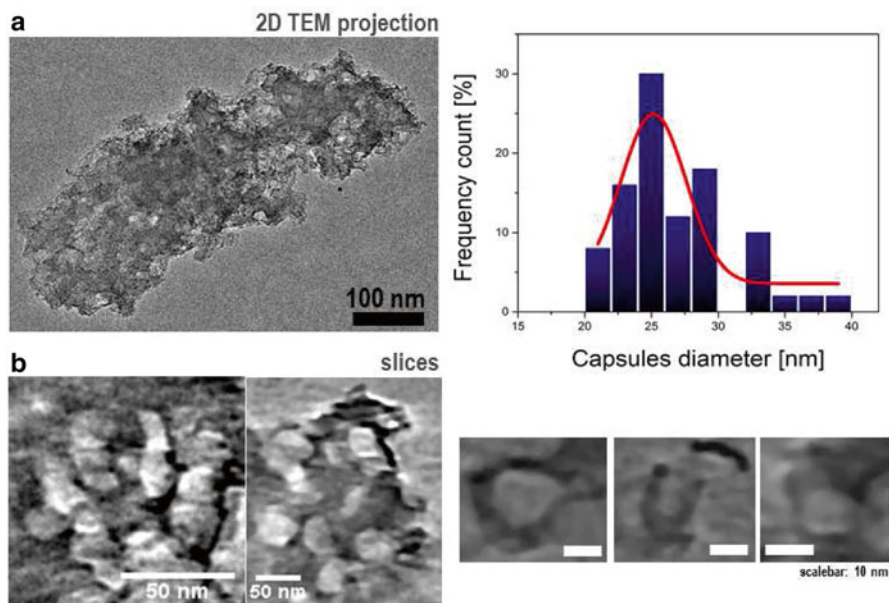


Fig. 6.16 Electron tomography investigation of phospholipids-silica nanocapsules by cryo-TEM low-dose tomography. The arrangement and morphology of nanocapsule assemblies is difficult to explore by (a) 2D cryo-TEM, whereas (b) volume slicing allowed the direct visualisation of nanocapsule size, shape and spatial arrangement. Reprinted from Cazelles et al. [54]

6.4.6 3D Studies of Physical Properties: Advanced Tomography

Atomically Resolved Tomography: Gold Nanorods

Significant progress has recently been achieved to obtain atomic resolution in 3D. As a matter of fact, the electron tomography at the atom scale offers the possibility not only to probe crystallographic details but to explore other physical properties such as the strains within 3D nano-objects [10, 55–57]. For instance, the group of Antwerp carried out these kinds of experiments on free-standing gold nanorods [55]. They deeply analysed these nanoparticles in 3D, collecting four different high-resolution HAADF-STEM images along different zone axes ([100], [110], [010] and [1-10]) and applying a compressive-sensing-based 3D reconstruction algorithm. Thus, the surface facets of the nanorods, as well as the surface relaxation, were investigated with high precision. From these analyses the authors concluded that these nanorods are mainly composed of {110} and {100} facets (Fig. 6.17a, b), and they also observed the presence of an atomic surface step (Fig. 6.17c), which can have an influence in the properties (catalytic, optical/electronic, mechanical) of these nanoparticles. In addition, they applied the

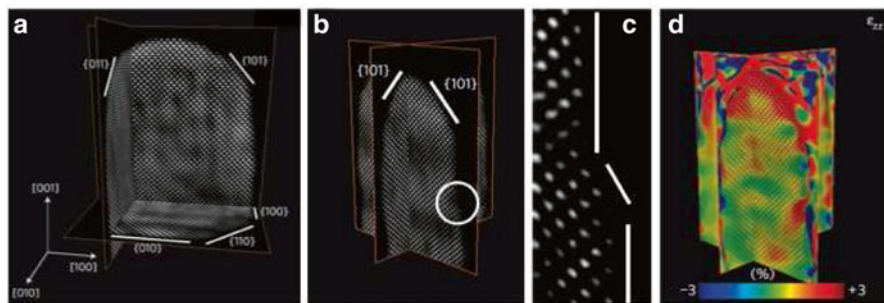


Fig. 6.17 (a) Three orthogonal slices through the reconstruction of a nanorod, showing individual atom positions. It can be seen that $\{110\}$ and $\{100\}$ facets compose the morphology of the rod. The tip is rounded, with clear terraces at the $\{101\}$ planes. (b) The tip of another nanorod is composed of $\{101\}$ facets. A region with an atomic surface step is indicated. (c) A more detailed view of the region circled in (b). In this region, a surface step with a thickness of two atoms is observed in the tomographic reconstruction. (d) Slices through the 3D ε_{zz} strain measurement indicating an outward relaxation of the atoms at the tip of the nanorod. Adapted from Goris et al. [55]

geometrical phase analysis (GPA) to the 3D reconstruction, and they obtained the full 3D ε_{zz} strain field (Fig. 6.17d). The colour code in Fig. 6.17d corresponds to the strain in the nanorod and is scaled between -3% and $+3\%$. This map revealed the anisotropy present in the ε_{zz} strain, which again, as also the authors pointed out, could have a significant impact on the optical response of these nanomaterials.

Plasmonic 3D Studies via STEM-EELS Tomography: Silver Nanocubes

In the recent years significant attention has been devoted to the study of noble metallic nanoparticles due to their optical response, which is related to the SPRs. It is well known that particle size, shape and composition, as well as the local dielectric environment of these nanoparticles, have strong impact on these SPRs [36–39, 48]. The combination of a precise 3D morphology and the distribution, at the nanoscale, of each SPR, provides very significant knowledge about the optical response of nanomaterials. In order to get this kind of information, the group of Cambridge developed monochromated STEM-EELS spectrum-imaging (SPIM) with a novel combination of non-negative matrix factorisation (NMF), compressed sensing and electron tomography [39]. Thus, they reconstructed a 3D image of the dominant SPR modes for an individual silver nanocube. These authors acquired STEM-EELS SPIMs at 5 different tilt angles (ranging from -60° to 0° , with 15° step, as they took advantage of the 4 mm symmetry of the Ag nanocube), tilting about a $\langle 100 \rangle$ cube axis perpendicular to the electron beam. Using NMF, they performed a blind separation between the different peaks in the STEM-EELS SPIMs and obtained five dominant SPRs for the Ag nanocube and their corresponding 2D maps at each tilt angle. Finally, they employed an iterative compressed sensing tomographic algorithm for obtaining the 3D reconstruction of the distribution of the SPRs (see Fig. 6.18).

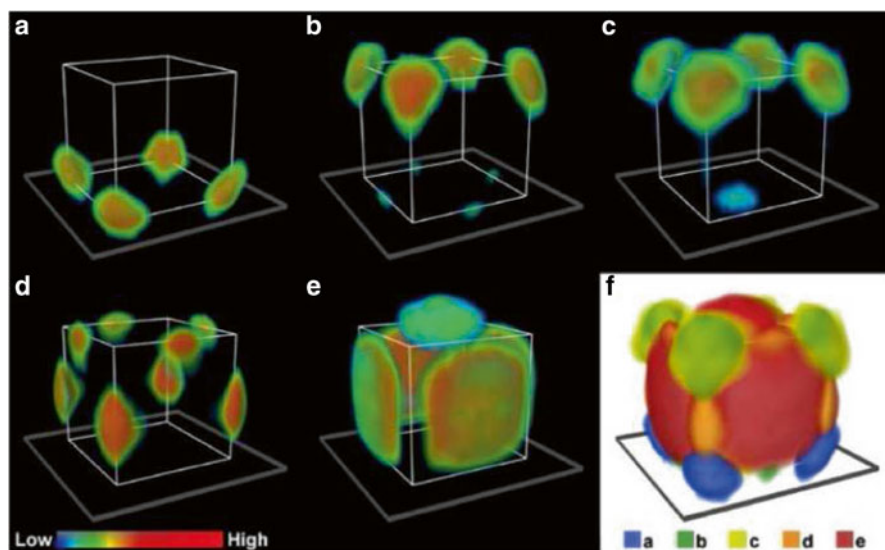


Fig. 6.18 3D visualisation of the SPR modes of an Ag nanocube. The 3D images displayed in (a–e) were obtained by tomographic reconstruction of the EELS maps of the respective five SPR modes identified by NMF. The visualisations are voxel projections of the reconstructed 3D volumes. The colour bar indicates the SPR intensity. (f) Combined 3D rendering of all the modes. Reprinted from Nicoletti et al. [39]

6.5 Conclusions and Perspectives

During the last decades, the material research community has paid increasing attention to the synthesis and the development of nanomaterials, leaving aside the development of means, methods and tools for the complete characterisation, including in 3D, of such objects and structures. We have shown in this review that full characterisation of nanomaterials, nano-objects and complex hybrid nano-systems can be achieved by means of electron microscopy. The electron tomography is the appropriate tool for a complete three-dimensional characterisation, whereas the in situ microscopy can provide key answers on questions relating the material structure and morphology to their behaviour under specific functioning conditions. The methods and approaches described herein are becoming more and more popular for they provide the direct relationship between material characteristics and their performances.

Owing to the variety of recording modes available in a TEM, modes experimentally adaptable to tomography, the 3D information gained covers key issues from nanomaterial morphology to elemental mapping. For instance, the quantitative tomography allows to carry out both qualitative and quantitative evaluations of nano-object porosity, e.g. to ascertain whether we deal with micro- or mesoporous

objects, to explore the pores connectivity, to estimate the porous volumes and/or surface areas and so on. It is the only technique capable to check whether nano-objects lie inside or outside hollow structures or to explore the location and distribution of nanoparticles and/or atomic clusters relative to a support. In addition, it is well adapted to accurate morphological studies like nano-crystal faceting, and to a larger extent, it describes quantitatively short- and long-range orders. Certainly, different recording modes can be successfully combined to optimise the quality/quantity of data necessary to access the specific information.

By combining the electron energy loss spectroscopy with the 3D tomography, one accede the three-dimensional chemical information at the nanometre scale: analytical tomography. Two representative examples have been given in this review: (1) the study of industrial silica/alumina catalysers prepared by different methods and (2) assessment of Fe and Co distribution within mesoporous antiferromagnetic Co_3O_4 nanocast replicas of SiO_2 KIT-6 templates filled with $\text{Fe}_x\text{Co}_{(3-x)}\text{O}_4$. These approaches have been used to establish the correlation between the morphology of the object, the 3D relative distribution of the elements and its catalytic performance. Although the analytical tomography is a rather volume-selective technique, it gives a clear representation of nanocomposite surface properties as correlated with the surface chemical selectivity. The close correspondence between morphology and chemical composition provides a powerful tool for the analysis of materials at the forefront in catalysis, nano-electronics, therapy or imaging. The analytical tomography is hence expected to have a strong impact in these fields' research in the very next future.

The recent progress in electron microscopy instrumentation and the development of new methodologies pave the path for the development of routine electron tomography with atomic resolution. Only a visionary project in the early 2000s, this vision is becoming more and more realistic, and it will certainly become a reality in the very next future. Further improvements are still needed though, as one first challenge will be to reduce the number of projections needed for obtaining reliable results. In principle, one should be able to increase the SNR in the acquired projections or to access more fragile materials by diminishing the total irradiation dose during the acquisition. A reliable solution to this problem can be the hardware implementation of compressed sensing. There's however one more provocative task to perform, maybe the most challenging one: the implementation of all characterisation techniques on the production chain of nanomaterials, no matter the applications envisioned.

Acknowledgements S.M. and O.E. acknowledge the French electron microscopy and atom probe network METSA. Prof. Clement Sanchez and his research group at Collège de France are acknowledged. We acknowledge the support received from the European Union Seventh Framework Program under Grant Agreement 312483—ESTEEM2 (Integrated Infrastructure Initiative—I3). R.A. acknowledges funding from the Spanish Ministerio de Economía y Competitividad (FIS2013-46159-C3-3-P).

References

1. J. Radon, Ben. Vehr. K. Sächs. Ges. Wiss. Leipzig Math-Phys. Kl. **69**, 262 (1917)
2. D. DeRosier, A. Klug, Reconstruction of three dimensional structures from electron micrographs. *Nature* **217**, 130 (1968)
3. A. Klug, From macromolecules to biological assemblies (Nobel lecture). *Angew. Chem. Int. Ed.* **22**, 565 (1983)
4. O. Medalia, I. Weber, A.S. Frangakis, D. Nicastro, G. Gerisch, W. Baumeister, Macromolecular architecture in eukaryotic cells visualized by cryoelectron tomography. *Science* **298**, 1209 (2002)
5. H. Jinnai, Y. Nishikawa, R.J. Spontak, S.D. Smith, D.A. Agard, T. Hashimoto, Direct measurement of interfacial curvature distributions in a bicontinuous block copolymer morphology. *Phys. Rev. Lett.* **84**, 518 (2000)
6. Y. Zhao et al., Small-molecule-directed nanoparticle assembly towards stimuli-responsive nanocomposites. *Nat. Mater.* **8**, 979 (2009)
7. A.J. Kloster et al., Three-dimensional transmission electron microscopy: a novel imaging and characterization technique with nanometer scale resolution for materials science. *J. Phys. Chem. B* **104**, 9368 (2000)
8. W.L. Ling et al., *J. Nanopart. Res.* **14**, 806 (2011)
9. D. Vanhecke et al., Cryo-electron tomography: methodology, developments and biological applications. *J. Microsc.* **242**, 221 (2011)
10. M.C. Scott, C.C. Chen, M. Mecklenburg, C. Zhu, R. Xu, P. Ercius, U. Dahmen, B.C. Regan, J. Miao, Electron tomography at 2.4 angstrom resolution. *Nature* **483**, 444 (2012)
11. K. Jarausch et al., Four-dimensional STEM-EELS: enabling nano-scale chemical tomography. *Ultramicroscopy* **109**, 326 (2009)
12. L. Yedra et al., EEL spectroscopic tomography: towards a new dimension in materials analysis. *Ultramicroscopy* **122**, 12 (2012)
13. S. Goris et al., Monitoring galvanic replacement through three-dimensional morphological and chemical mapping. *Nano Lett.* **14**, 3220 (2014)
14. A.H. Janssen, A.J. Koster, K.P. de Jong, Three-dimensional transmission electron microscopic observations of mesopores in dealuminated zeolite Y. *Angew. Chem. Int. Ed.* **40**, 1102 (2001)
15. O. Ersen, J. Werckmann, M. Houllé, M.-J. Ledoux, C. Pham-Huu, 3D electron microscopy study of metal particles inside multiwalled carbon nanotubes. *Nano Lett.* **7**, 1898 (2007)
16. O. Ersen, C. Hirlimann, M. Drillon, J. Werckmann, F. Tihay, C. Pham-Huu, C. Crucifix, P. Schultz, 3D-TEM characterization of nanometric objects. *Solid State Sci.* **9**, 1088 (2007)
17. H. Friedrich, J.R.A. Sietsma, P.E. de Jongh, A.J. Verkleij, K.P. de Jong, Measuring location, size, distribution, and loading of NiO crystallites in individual SBA-15 pores by electron tomography. *J. Am. Chem. Soc.* **129**, 10249 (2007)
18. P.A. Midgley, M. Weyland, J.M. Thomas, B.F.G. Johnson, Z-Contrast tomography: a technique in three-dimensional nanostructural analysis based on Rutherford scattering. *Chem. Commun.* **10**, 907 (2001)
19. P.A. Midgley, M. Weyland, 3D electron microscopy in the physical sciences: the development of Z-contrast and EFTEM tomography. *Ultramicroscopy* **96**, 413 (2003)
20. G. Mobus, R.C. Doole, B.J. Inkson, Spectroscopic electron tomography. *Ultramicroscopy* **96**, 433 (2003)
21. L. Roiban, L. Sorbier, C. Pichon, P. Bayle-Guillemaud, J. Werckmann, M. Drillon, O. Ersen, Three-dimensional chemistry of multiphase nanomaterials by energy-filtered transmission electron microscopy tomography. *Microsc. Microanal.* **18**, 1118 (2012)
22. I. Florea, A. Demortière, C. Petit, H. Bulou, C. Hirlimann, O. Ersen, Electron tomography and 3D molecular simulations of platinum nanocrystals. *Nanoscale* **2**, 2668 (2010)
23. P.A. Midgley, E.P.W. Ward, A.B. Hungria, J.M. Thomas, Nanotomography in the chemical, biological and materials sciences. *Chem. Soc. Rev.* **36**, 1477 (2007)
24. P.A. Midgley, C. Durkan, The frontiers of microscopy. *Mater. Today* **11**, 8 (2008)

25. J. Frank, B.F. McEwan (eds.), (Plenum, New York, 1992), p. 91
26. M.H. Gass, K.K.K. Koziol, A.H. Windle, P.A. Midgley, Four-dimensional spectral tomography of carbonaceous nanocomposites. *Nano Lett.* **6**(3), 376 (2006)
27. G. Möbus, B.J. Inkson, Three-dimensional reconstruction of buried nanoparticles by element-sensitive tomography based on in elastically scattered electrons. *Appl. Phys. Lett.* **79**, 1369 (2001)
28. M. Radermacher, Radon transform techniques for alignment and three-dimensional reconstruction. *Scanning Microsc.* **11**, 171 (1997)
29. K.J. Batenburg, S. Bals, J. Sijbers, C. Kübel, P.A. Midgley, J.C. Hernandez, U. Kaiser, E.R. Encina, E.A. Coronado, G. Van Tendeloo, 3D imaging of nanomaterials by discrete tomography. *Ultramicroscopy* **109**, 730 (2009)
30. G.L. Zeng, Image reconstruction—a tutorial. *Comput. Med. Imaging Graph.* **25**, 97 (2001)
31. W.O. Saxton, What is the focus variation method—is it new—is it direct. *Ultramicroscopy* **13**, 57 (1984)
32. R.A. Crowther, D.J. DeRosier, A. Klug, The reconstruction of a three-dimensional structure from projections and its application to electron microscopy. *Proc. R. Soc. Lond. A* **317**, 319 (1970)
33. R. Gordon, R. Bender, G.T. Herman, Algebraic reconstruction techniques (ART) for three-dimensional electron microscopy and x-ray photography. *J. Theor. Biol.* **24**, 471 (1970)
34. P. Gilbert, Iterative methods for the three-dimensional reconstruction of an object from projections. *J. Theor. Biol.* **36**, 105 (1972)
35. Z. Saghi, D.J. Holland, R. Leary, A. Falqui, G. Bertoni, A.J. Sederman, L.F. Gladden, P.A. Midgley, Three-dimensional morphology of iron oxide nanoparticles with reactive concave surfaces. A compressed sensing-electron tomography (CS-ET) approach. *Nano Lett.* **11**, 4666 (2011)
36. L. Novotny, B. Hecht, *Principles of Nano-Optics* (Cambridge University Press, Cambridge, 2006)
37. S.A. Maier, *Plasmonics: Fundamentals and Applications* (Springer, Berlin, 2007)
38. L.M. Liz-Marzan, *Langmuir* **22**, 32–41 (2006)
39. O. Nicoletti, F. de la Peña, R.K. Leary, D.J. Holland, C. Ducati, P.A. Midgley, Three-dimensional imaging of localized surface plasmon resonances of metal nanoparticles. *Nature* **502**, 80–84 (2013)
40. L. Borowik, I. Florea, D. Deresmes, O. Ersen, D. Hourlier, T. Mélin, Surface and intrinsic conduction properties of Au-catalyzed Si nanowires. *J. Phys. Chem. C* **116**, 6601–6607 (2012)
41. I. Janowska, F. Vigneron, D. Bégin, O. Ersen, P. Bernhardt, T. Romero, M.J. Ledoux, C. Pham-Huu, Mechanical thinning to make few-layer graphene from pencil lead. *Carbon* **50**, 3092 (2012)
42. A. Ciesielski, S. Haar, M. El Gemayel, H. Yang, J. Clough, G. Melinte, M. Gobbi, E. Orgiu, M.V. Nardi, G. Ligorio, V. Palermo, N. Koch, O. Ersen, C. Casiraghi, P. Samori, Harnessing the liquid-phase exfoliation of graphene using aliphatic compounds: a supramolecular approach. *Angew. Chem. Int. Ed.* **53**(39), 10355 (2014)
43. I. Janowska, O. Ersen, T. Jacob, P. Venegues, D. Begin, M.J. Ledoux, C. Pham-Huu, Catalytic unzipping of carbon nanotubes to few-layer graphene sheets under microwaves irradiation. *Appl. Catal. A* **371**, 22 (2009)
44. G. Melinte, I. Florea, S. Moldovan, I. Janowska, W. Baaziz, R. Arenal, A. Wisnet, C. Scheu, S. Begin-Colin, D. Begin, C. Pham-Huu, O. Ersen, A 3D insight on the catalytic nanostructure of few-layer graphene. *Nat. Commun.* **5**, 4109 (2014)
45. D. Ihiwakrim, O. Ersen, F. Melin, P. Hellwig, I. Janowska, D. Begin, W. Baaziz, S. Begin, C. Pham-Huu, R. Baati, Non-covalent functionalization of graphene with hexahistidine-pyrene amphiphiles in water: stepwise construction of 2D-nanostructured composites with iron oxide nanoparticles. *Nanoscale* **5**, 9073 (2013)
46. T. Fontecave, C. Sanchez, T. Azais, C. Boissiere, Chemical modification as a versatile tool for tuning stability of silica based mesoporous carriers in biologically relevant conditions. *Chem. Mater.* **24**, 4326 (2012)

47. T. Fontecave, C. Boissiere, N. Baccile, F.J. Plou, C. Sanchez, Using evaporation-induced self-assembly for the direct drug templating of therapeutic vectors with high loading fractions, tunable drug release, and controlled degradation. *Chem. Mater.* **25**, 4671 (2013)
48. R. Arenal, L. Henrard, L. Roiban, O. Ersen, J. Burgin, M. Treguer-Delapierre, Local plasmonic studies on individual core-shell gold–silver and pure gold nano-bipyramids. *J. Phys. Chem. C* **118**, 25643–25650 (2014)
49. V. Pierron-Bohnes, I. Florea, O. Ersen, C. Ulhaq-Bouillet, C. Goyhenex, N. Briday, C. Ricolleau, Y. Le Bouar, D. Alloyeau, Atomic-scale faceting in CoPt nanoparticles epitaxially grown on NaCl. *Cryst. Growth Des.* **14**(5), 2201 (2014)
50. Baaziz, I. Florea, S. Moldovan, V. Papaefthimiou, S. Zafeiratos, S. Begin-Colin, D. Begin, O. Ersen, C. Pham-Huu, Microscopy investigations of the microstructural change and thermal response of cobalt-based nanoparticles confined inside a carbon nanotube medium. *J. Mater. Chem. A.* (2015). doi:[10.1039/C5TA00283D](https://doi.org/10.1039/C5TA00283D)
51. M.S. Moldovan, H. Bulou, Y.J. Dappe, I. Janowska, D. Begin, C. Pham-Huu, O. Ersen, On the evolution of Pt nanoparticles on few-layer graphene supports in the high-temperature range. *J. Phys. Chem. C* **116**, 9274 (2012)
52. J.-Y. Bigot, H. Kesserwan, V. Halté, O. Ersen, M.S. Moldovan, T.H. Kim, J.-t. Jang, J. Cheon, Magnetic properties of annealed core-shell CoPt nanoparticles. *Nano Lett.* **12**, 1189 (2012)
53. R. Arenal, F. de la Pena, O. Stephan, M. Walls, M. Tence, A. Loiseau, C. Colliex, Extending the analysis of EELS spectrum-imaging data, from elemental to bond mapping in complex nanostructures. *Ultramicroscopy* **109**, 32 (2008)
54. R. Cazelles, J. Drone, F. Fajula, O. Ersen, S. Moldovan, A. Galarneau, Reduction of CO₂ to methanol by a polyenzymatic system encapsulated in phospholipids–silica nanocapsules. *New J. Chem.* **37**, 3721 (2013)
55. B. Goris, S. Bals, W. Van den Broek, E. Carbó-Argibay, S. Gómez-Graña, L.M. Liz-Marzán, G. Van Tendeloo, Atomic-scale determination of surface facets in gold nanorods. *Nat. Mater.* **11**, 930 (2012)
56. S. Van Aert, K.J. Batenburg, M.D. Rossell, R. Erni, G. Van Tendeloo, Three-dimensional atomic imaging of crystalline nanoparticles. *Nature* **470**, 374–377 (2011)
57. S. Bals et al., Three-dimensional atomic imaging of colloidal core-shell nanocrystals. *Nano Lett.* **11**, 3420–3424 (2011)